Supramolecular Assembly of Halide Perovskite Building Blocks

Cheng Zhu,[1,3,5] Jianbo Jin,[2,5] Mengyu Gao,[1,3,5] Alexander M. Oddo,[2,3] Maria C. Folgueras,[1,3] Ye Zhang,[2] Chung-Kuan Lin,[2,3] and Peidong Yang[1,2,3,4,*]

1. Department of Materials Science and Engineering, University of California, Berkeley, California 94720, USA.

2. Department of Chemistry, University of California, Berkeley, California 94720, USA.

3. Materials Sciences Division, Lawrence Berkeley National Laboratory, Berkeley, California 94720, USA.

4. Kavli Energy NanoScience Institute, Berkeley, California 94720, USA.

5. These authors contributed equally.

* Correspondence: p_yang@berkeley.edu

ABSTRACT

The structural diversity and tunable optoelectronic properties of halide perovskites originate from the rich chemistry of metal halide ionic octahedron $[MX_6]^{n-}$ (M = Pb^{2+}, Sb^{3+}, Te^{4+}, Sn^{4+}, Pt^{4+}, etc.; X = Cl^-, Br^-, I^-). The properties of the extended perovskite solids are dictated by the assembly, connectivity, and interaction of these octahedra within the lattice environment. Hence, the ability to manipulate and control the assembly of the octahedral building blocks is paramount for constructing new perovskite materials. Here, we propose a systematic supramolecular strategy for the assembly of $[MX_6]^{n-}$ octahedra into a solid extended network. Interaction of alkali metal-bound crown ethers with $[M(IV)X_6]^{2-}$ octahedron resulted in a structurally and optoelectronically tunable "dumbbell" structural unit in solution. Single crystals with diverse packing geometries and symmetries will form as the solid assembly of this new supramolecular building block. This supramolecular assembly route introduces a new general strategy for designing halide perovskite structures with potentially new optoelectronic properties.

INTRODUCTION

Halide perovskite has been the spotlight of semiconductor research in the past decade owing to its superior optoelectronic properties: high optical absorption coefficient, tunable bandgap, long free carrier diffusion length, high defect tolerance and efficient photo/electro-luminescence.[1,2] There are increasing studies revealing the fact that the $[MX_6]^{n-}$ (M = Pb^{2+},[3-5] Sb^{3+},[6-8] Te^{4+},[9-11] Sn^{4+},[12,13] Pt^{4+},[14] etc.; X = Cl^-, Br^-, I^-) metal halide ionic octahedral units are the fundamental building blocks and functional units in metal halide perovskites. To this end, metal halide perovskites can be described as the extended assembly of those octahedra balanced by counter cations.[14,15] In this work, we introduce supramolecular cations as the counter cations for constructing the metal halide octahedron assembly. Crown ether can readily coordinate with alkali metals to form crown ether@alkali metal cations that have been widely used for supramolecular assembly.[16,17] Various assemblies of polyoxometalate clusters[18] and metal halide clusters, such as the five-coordinate $[SbX_5]^{2-}$ complex[19] or the four-coordinate $[FeCl_4]^{-}$[20] and $[MnBr_4]^{2-}$[21] complexes, can be formed by employing different crown ether@alkali metal complexes. Here we show that the assembly of metal halide octahedron results in a family of unique dumbbell-shaped (crown ether@A)$_2$M(IV)X_6 (crown ether = 18-Crown-6 (18C6), 21-Crown-7 (21C7); A = Cs^+, Rb^+, K^+; M = Te^{4+}, Sn^{4+}, Se^{4+}, Ir^{4+}, Pt^{4+}, Zr^{4+}, Ce^{4+}; X = Cl^-, Br^-, I^-) structural units in solution, which can be further packed into various three-dimensional crystal structures. Moreover, the optoelectronic properties of the resulted assembly can be tuned by using different building units, providing an additional knob for the rational design of functional metal halide perovskites.

Previous works have shown, that upon dissolving bulk $A_2M(IV)X_6$ vacancy-ordered double perovskites in polar aprotic solvents, the ionic bond between the $[M(IV)X_6]^{2-}$ and the alkali metal cations (A^+) dissociates, and the metal halide octahedral units can be stabilized in solution.[22]

Additionally, when 18C6 was dissolved in solution, the strong electrostatic interaction between the alkali metal cations A^+ and the oxygen atoms of 18C6 favored $(18C6@A)^+$ cation formation.[23,24] Furthermore, we discovered that the $[M(IV)X_6]^{2-}$ octahedra and the $(18C6@A)^+$ cations in solution self-assemble into a $(18C6@A)_2M(IV)X_6$ dumbbell structural unit, where each octahedron is sandwiched by two $(18C6@A)^+$ cations (Figure 1). This configuration lays the foundation for solid-state supramolecular assembly. Using the anti-solvent vapor assisted crystallization method (Figure S1), the dumbbell building blocks packed into a unique rhombohedral lattice (Figure 1), which is different from the face-centered cubic (FCC)-type lattice formed by $[M(IV)X_6]^{2-}$ and A^+ alone. This new, general synthetic strategy allows us to build up a family of new supramolecular structures based upon these metal halide octahedral building blocks.

RESULTS AND DISCUSSION

Structural Unit Formation in Solution. The charge-neutral $(18C6@A)_2M(IV)X_6$ dumbbell structural units are formed by dissolving 18C6 and $A_2M(IV)X_6$ in acetonitrile (ACN). This was verified by multiple solution-state characterization techniques, using $(18C6@Cs)_2TeBr_6$ as an illustrating example. The NMR-active ^1H, ^{79}Br, and ^{133}Cs nuclei in the dumbbell structural unit experience different magnetic fields compared to the isolated nuclei (Figure 2a-c). The 24 homotopic protons on the 18C6 ring have identical NMR absorptions, at around 3.54 ppm in terms of chemical shift. Once a Cs^+ is crowned, due to the partial removal of proton electron density by the cation, the protons will be deshielded and the chemical shift will increase to 3.59 ppm (Figure 2a), consistent with reports that $(18C6@Cs)^+$ exists in ACN.[23] However, with the addition of $[TeBr_6]^{2-}$ ionic octahedra, the chemical shift is further increased to 3.61 ppm. This increase indicated further withdrawal of electron density from the protons in the presence of $[TeBr_6]^{2-}$,

which implied attachment to the $(18C6@Cs)^+$ cations. ^{79}Br NMR revealed strong signals of free Br^- ions of CsBr in ACN, while the spin relaxation of ^{79}Br was quenched completely by Te^{4+} in Cs_2TeBr_6 (Figure 2b) under the same measurement conditions most likely due to quadrupolar interaction.[25] $(18C6@Cs)_2TeBr_6$ in ACN showed the same quenching behavior as the Cs_2TeBr_6; the absence of ^{79}Br NMR signal confirmed that Br was coordinated to Te^{4+}.

To provide evidence that the dumbbell structural unit exists in ACN, ^{133}Cs NMR (Figure 2c) was also conducted since Cs is the bridging atom that directly coordinates to both, Br of $[TeBr_6]^{2-}$ and O of 18C6. The free Cs chemical shift of CsBr was located at 38.81 ppm, while it was located at 35.56 ppm for Cs_2TeBr_6 in ACN. The 3.25-ppm difference in these controls indicated that the presence of Te^{4+} in the solution caused the peak to shift to lower ppm values. In contrast, a pronounced shielding effect was observed when Cs^+ was crowned into $(18C6@Cs)^+$ in ACN, which suggested a withdrawal of electron density from the crown ether to Cs^+, consistent with the ^1H NMR results. Adding $[TeBr_6]^{2-}$ into $(18C6@Cs)^+$ in ACN changed the Cs chemical shift from 22.22 ppm to 22.97 ppm, which supported the formation of a new species, the dumbbell structural unit, distinct from its individual components. The dramatically broadened signal also supported the formation of the dumbbell, as dipole-dipole interactions are introduced in slowly tumbling large molecular weight species. UV-vis spectrum of $(18C6@Cs)_2TeBr_6$ precursors in ACN clearly shows the A, B and C characteristic absorption bands of $[TeBr_6]^{2-}$ (Figure 2d),[22] indicating the presence of the $[TeBr_6]^{2-}$ in solution. With the comprehensive measurements in ^1H, ^{79}Br, and ^{133}Cs NMR and UV-vis spectroscopy, we characterized the species in the solution phase, confirming the integrity of the dumbbell structural unit in solution (Figure 1).

Single Crystal Characterization. With the suspension of $(18C6@A)_2M(IV)X_6$ units in ACN solution, we successfully achieved the solid-state assembly, in the form of single crystals, with the

introduction of antisolvents like diethyl ether. For example, the $(18C6@Cs)_2TeCl_6$ single crystals have a parallelepiped shape, consistent with crystallographic symmetry, with a lateral dimension of approximately 300 μm (Figure S2). The structural details of the crystals were determined from single crystal X-ray diffractions (SCXRD). $(18C6@Cs)_2TeCl_6$ crystallized in the R-3 space group with lattice parameters of a = 13.9378 Å and c = 22.0396 Å (Table S1). The $(18C6@Cs)_2TeCl_6$ dumbbell structural unit belonged to the S_6 point group, where two Cs^+ cations and the Te^{4+} cation sit on the S_6 axis, and the six-fold symmetry of the 18C6 and S_6 axis of O_h-symmetric $[TeCl_6]^{2-}$ octahedron were perfectly aligned. In the $(18C6@Cs)_2TeCl_6$ dumbbell unit, the Te-Cl bond length was determined as 2.546 Å, which was comparable to that in the Cs_2TeCl_6 vacancy-ordered double perovskite (2.570 Å).[9] The high symmetry of this dumbbell building block offered a unique rhombohedral packing of the octahedra at the macroscopic level. Each $[TeCl_6]^{2-}$ octahedron occupied the b Wyckoff position of space group R-3 and was surrounded by six nearest octahedra at a Te-Te distance of 10.9 Å, which was different from the FCC packing in Cs_2TeCl_6 with Te-Te distance of 7.7 Å.[9] The voids within the lattice are occupied by disordered solvent molecules. These tunable differences in the metal halide octahedron packing geometry may lead to differences in the overlap of molecular orbital wavefunctions, yielding unique electronic structures and optoelectronic properties that will be discussed later.

Tunability of the Supramolecular Approach. To demonstrate the general applicability of our approach, we produced various crystals through this supramolecular assembly strategy. In fact, the composition tunability of this new $(18C6@A)_2M(IV)X_6$ structure is as rich as the tunabilities on A, M, and X sites in $A_2M(IV)X_6$ double perovskites.[26] There are four compositional components in the $(18C6@Cs)_2TeCl_6$ dumbbell structural unit that can be tuned by virtue of the precursors: (a) octahedron cations (M), (b) halide anions (X), (c) alkali metal cations (A), and (d) crown ethers

(Figure 3). Apart from the $[TeX_6]^{2-}$, various tetravalent center cation octahedra, such as $[SnX_6]^{2-}$, $[SeX_6]^{2-}$, $[IrX_6]^{2-}$, $[PtX_6]^{2-}$, $[ZrX_6]^{2-}$, $[CeX_6]^{2-}$,[12,13,27-35] can also be assembled into similar dumbbell structural units with S_6 symmetry. For typical 3D-connected halide perovskites, such as low-T phase $CsPbI_3$,[36] due to the geometrical constraint imposed by the ionic framework sizes, such as the tolerance factor and proper bonding directions, a mismatched ionic size will lead to the breakdown or instability of the perovskite structure.[37] In contrast, the isolated nature of the dumbbell structural units enables a more flexible control over the structure diversity without losing the prototypical crystal structure. Herein, we achieve a variety of unique dumbbell structures with our unique synthetic approach by simply changing the precursors. All structural details of the highly tunable $(18C6@A)_2M(IV)X_6$ dumbbell structural units were obtained by powder X-ray diffraction (PXRD) and SCXRD (Table S1-S7).

The comparison of PXRD patterns for the seven different octahedron center cations (Te^{4+}, Sn^{4+}, Se^{4+}, Ir^{4+}, Pt^{4+}, Zr^{4+}, Ce^{4+}) is shown in Figure 4a. Despite size differences between the different metal halide octahedral units, represented by the M-Cl bond length (from 2.324 Å to 2.555 Å) summarized in Figure 4b, they all had similar hexagonal PXRD patterns, with strong and distinct (101) and (110) diffraction peaks. In order to better evaluate the geometry of the dumbbell structural unit with various composition, we used a simplified model made up with two cones and one octahedron (Figure S3). A larger halide anion (from Cl^- to Br^- to I^-) leads to a larger octahedron size (Figure 4d), and the length of the dumbbell structural unit increases in all three dimensions, reflected by the shifting of all diffraction peaks to lower 2θ values (Figure 4c). While the bromide version remained in the R-3 space group (Table S2), the iodide version deviated from the hexagonal symmetry and crystallized in the monoclinic crystal system with the space group of $P2_1/m$ (Table S7 and Figure S4) due to the larger size of the iodide anion. On the contrary, we

found that the M-X bonds were not influenced by the alkali metal cations, and the R-3 space group can be preserved. Figure 4f shows that the Te-Cl bond lengths were 2.546 Å, 2.548 Å, and 2.544 Å for the Cs-, Rb- and K-based assemblies, respectively. However, when using a smaller alkali cation, the height of the cone decreased (from ~2.4 Å to ~1.8 Å when changing from Cs^+ to K^+), while the diameter of the cone remained nearly unchanged. This height decrease was consistent with a shift in the diffraction peaks related to the c lattice parameter (such as (101) and (104) planes) to larger 2θ values. In contrast, the diffraction of facets parallel to the c axis, such as the (110) plane, have almost no shift (Figure 4e and Figure S5 and S6). We also compared the single crystals of $(18C6@K)_2TeBr_6$ synthesized from ACN and DMF (Table S8), both crystals are in the R-3 space group and only show slight differences in lattice parameters, which are attributed to the occupation of disordered larger DMF molecules compared to ACN molecules in the voids within the lattice. Thermogravimetric analysis (TGA) on $(18C6@Cs)_2TeCl_6$ shows the total relative mass changes from 98.5% (M_w = 1248.95 g/mol for $(18C6@Cs)_2TeCl_6 \cdot 2DMF$) to 88.6% ($M_w$ = 1134.76 g/mol for $(18C6@Cs)_2TeCl_6$) from 80℃ to 120℃, and further reduced to 48.9% (M_w = 606.13 g/mol for Cs_2TeCl_6) from 160℃ to 220℃. (Figure S7) The same decomposition process is also verified for $(18C6@Cs)_2SnCl_6$, and $(18C6@Cs)_2TeBr_6$. Thermal analysis studies reveal the fact that for this family of new materials, the solvent molecules (such as DMF) occupying the lattice voids is evaporated from 80℃ to 120℃, and 18C6 starts to detach at roughly 160℃ and completely decomposes into the corresponding all-inorganic Cs_2MX_6 powders after 220℃. It also proves the existence of solvent molecules in the lattice voids as we expected from the single crystal structure studies.

To further confirm the intact O_h symmetry of the metal halide octahedral building blocks, we used Raman spectroscopy to study the vibrational modes of the dumbbell structural unit. Previous

Raman studies of the Cs_2TeCl_6 crystal system determined that the vibrational units in the single crystals were the isolated $[TeCl_6]^{2-}$ octahedra with O_h point group symmetry (Figure S8).[9] All three characteristic Raman peaks were still observed in the $(18C6@A)_2TeCl_6$ single crystals (Figure S9), confirming the O_h symmetry of the $[TeCl_6]^{2-}$ unit in the dumbbell building block. Similar O_h symmetry Raman peaks were also observed in assembled crystals with other octahedra, such as $[TeBr_6]^{2-}$, $[SnCl_6]^{2-}$, and $[SnBr_6]^{2-}$ (Figure S10-S12).

The compatibility between the point groups of 18C6 and the metal halide octahedral units resulted in the rhombohedral R-3 space group of the assembled single crystals. By breaking the six-fold symmetry of the crown ether, the supramolecular approach can realize more packing geometries for these metal halide octahedral units. For example, the larger 21-Crown-7 (21C7) had to distort itself to coordinate with the center Cs^+ cation (Figure S13a). Such distortion of the dumbbell building block dramatically altered the packing geometry of those building blocks (Figure S13b, c). Single crystals of $(21C7@Cs)_2TeBr_6$ and $(21C7@Cs)_2TeI_6$ crystallized in an orthorhombic lattice with space group $Cmc2_1$ (Table S9). The $[TeBr_6]^{2-}$ units in $(21C7@Cs)_2TeBr_6$ dumbbell unit were still nearly perfect, but this distorted dumbbell structure was found to be horizontally packed into a 2-dimensional (2D) array form. In each $[TeBr_6]^{2-}$ octahedral plane, one octahedron had four nearest neighbors (Te-Te distance is 9.9 Å), with no solvent molecules or crown ether complexes in between. The interlayer spacing of the 2D octahedral sheets was about 13.7 Å. Consistent with a 2D structure, the (002) diffraction peak was much stronger than the other diffraction peaks (Figure S14). The single crystal had a planar shape with a width of over 400 μm and a thickness of only 35 μm (Figure S15 and S16). Therefore, the use of 21C7 introduced another new type of metal halide octahedral unit packing in our supramolecular assemblies.

Optoelectronic Properties of the Supramolecular Assemblies. The demonstrated synthetic flexibility and systematic control of the crystal structures assembled from the dumbbell structural unit have deep implications on their electronic properties. The electronic structure of the structural unit is primarily determined by the metal halide octahedral units.[14] For instance, by tuning the center metal cation of the $[M(IV)Cl_6]^{2-}$ ($M = Sn^{4+}$, Te^{4+}, Ce^{4+}, and Ir^{4+}) ionic octahedron, the optical absorption onset of the supramolecular assembled crystals varied from 660 nm for $[IrCl_6]^{2-}$, to 500 nm for $[CeCl_6]^{2-}$, to 460 nm for $[TeCl_6]^{2-}$, and to 310 nm for $[SnCl_6]^{2-}$ (Figure 5a). The differences in absorption features for these four ionic octahedra are due to their different electronic configurations. Te^{4+} is a cation with ns^2 electronic configuration; the absorbance of $[TeCl_6]^{2-}$ octahedra was dominated by the molecular 5s to 5s5p transitions, represented as the A, B, and C bands.[35] Recent studies suggested that sharp absorption band in the UV range for $[SnCl_6]^{2-}$ can be assigned to a ligand-to-metal charge transfer (LMCT) transition.[28,29] The absorption band was also assigned to the LMCT transition for $[CeCl_6]^{2-}$.[37] For Ir, the subshells of the 5d-orbitals of Ir^{4+} in $[IrCl_6]^{2-}$ contributed to the weak optical transition bands and intense bands were due to metal-ligand interactions.[40] Changing the halide anions also contributed to different optical absorption. $(18C6@Cs)_2TeX_6$ ($X = Cl^-$, Br^-, I^-) structural units have vastly different optical absorption features due to shift of the atomic orbital energy levels of halide anions (Figure 5b).

The optoelectronic tunability of the dumbbell unit can be achieved not only by incorporating various $[M(IV)X_6]^{2-}$ ionic octahedra, but also by changing the octahedral packing geometries and the surrounding coordination environment of the same metal-halide octahedra. The electronic interaction of these octahedral units has deep implications on the electronic structure of the crystal. According to the tight-binding model, the superposition of wave functions for isolated atoms will be greater when atoms are brought closer together in a solid, so the electronic bands will be more

dispersive and the bandgap will decrease.[41] In the current materials system, the individual octahedron can be viewed as a super ion/atom with specific molecular orbital levels. When the octahedra of these dumbbell units are closer to each other, their orbital wavefunctions will overlap to a greater extent. This was confirmed by our experimental observation. The UV-vis absorption spectra of four different packing geometries of $[TeBr_6]^{2-}$ octahedra are shown in Figure 5c. As the $[TeBr_6]^{2-}$ octahedra were packed closer in a crystal by using different crown ether complexes, the A band absorption onset red shifted from 500 nm to 590 nm, causing the crystal to change color from orange [$(18C6@Cs)_2TeBr_6$ and $(21C7@Cs)_2TeBr_6$] to red [Cs_2TeBr_6] (Figure S17).

The supramolecular assembled crystals have not only tunable optical absorption but also strong photoluminescence (PL) with highly tunable emission color. For instance, under 250 nm excitation, $(18C6@Cs)_2ZrCl_6$ displays an intense blue emission at 459 nm, with a full width at half maximum (FWHM) of 0.90 eV. The photoluminescence quantum yield (PLQY) of $(18C6@Cs)_2ZrCl_6$ is 12.57%, which is calculated from integrating sphere measurements. Apart from high emission intensities, the supramolecular approach can also enable the fine-tuning of the emission color. The strong coupling of the exciton with lattice vibrations will greatly lower the energy level of the exciton, forcing it into transient self-trapped exciton (STE) states with a range of self-trapped energy levels.[11,30,31,42,43] $[TeCl_6]^{2-}$ octahedron was selected to study the STE emission of the dumbbell structural units. The PL spectra (Figure 5d and Figure S18) of the $(18C6@A)_2TeCl_6$ (A = K^+, Rb^+, Cs^+) crystals had emission peak wavelengths at 604 nm, 642 nm, 659 nm, respectively. They all featured a large Stokes shift of 1.13 eV, 1.26 eV, 1.31 eV, respectively, and a very broadband emission. The PL FWHM were 0.44 eV, 0.54 eV, and 0.55 eV, respectively. The Stokes shift was larger than that of the Cs_2TeCl_6 crystal, with a value of 1.04 eV,[9] which indicated a greater exciton-phonon coupling effect.[42,43] Furthermore, the Stokes shift increased with

increasing alkali metal cation size. This phenomenon was likely due to the difference in the alkali metal-halide bond strength. A weaker or softer alkali metal-halide bond will force the excitonic state into deeper self-trapped levels. The PL studies demonstrate that the supramolecular assembly approach can be used to design emissive and tunable emitters.

CONCLUSION

In conclusion, we demonstrated a general synthetic strategy for a library of new supramolecular building blocks (crown-ether@A)$_2$M(IV)X$_6$, constructed from ionic halide perovskite octahedral units and crown ether. The great tunability of (crown-ether@A)$_2$M(IV)X$_6$ can be explored along: (1) changing the octahedron cation, (2) tuning the halide anion, (3) modifying the alkali metal cation coupled with the crown ether, and (4) varying the size of the crown ether. In the future, based on the structural diversity of the supramolecular assembly approach, we expect to extend to 1D and 2D electronic dimensionality solid assembly with connected $[MX_6]^{n-}$ octahedra. Also, with all these synthetic possibilities, a more in-depth study of the optoelectronic properties of the ionic octahedral building blocks can be conducted. We expect that this new assembly strategy of the supramolecular building blocks could bring a new general method for halide perovskite materials discovery.

ASSOCIATED CONTENT

Supporting Information

The Supporting Information is available free of charge at xxxxxxx-xxxxxxx

Description of experimental details and additional characterization data. Supplementary Tables 1-9 show single-crystal XRD crystallographic results. Supplementary Figures 1-17 includes schematics, optical images, SEM images, single-crystal XRD and powder XRD characterizations, Raman spectra, UV-vis spectra and PL spectra.

Accession Code

The crystallographic information file (CIF) has also been deposited in the Inorganic Crystal Structure Database under reference numbers CSD 2122190-2122206, and 2145197-2145199. These data can be obtained free of charge via https://www.ccdc.cam.ac.uk/structures/, or by emailing data_request@ccdc.cam.ac.uk.

AUTHOR INFORMATION

Corresponding Author

Peidong Yang: p_yang@berkeley.edu

Authors

Cheng Zhu: cheng_zhu@berkeley.edu

Jianbo Jin: jianbo_jin@berkeley.edu

Mengyu Gao: mygao@berkeley.edu

Alexander M. Oddo: alex_oddo@berkeley.edu

Maria C. Folgueras: mcf26@berkeley.edu

Ye Zhang: ye_zhang@berkeley.edu

Chung-Kuan Lin: cklin@berkeley.edu

ORCID

Cheng Zhu: 0000-0001-6649-7812

Jianbo Jin: 0000-0002-9054-7960

Mengyu Gao: 0000-0003-1385-7364

Alexander M. Oddo: 0000-0002-5458-8650

Maria C. Folgueras: 0000-0001-6502-7616

Ye Zhang: 0000-0001-5953-2173

Chung-Kuan Lin: 0000-0001-9193-2345

Peidong Yang: 0000-0003-4799-1684

Author Contributions

C.Z., J.J. and M.G. made equal contribution to this study. The authors declare no competing financial interest.

Notes

The authors declare no competing financial interest.

ACKNOWLEDGMENTS

The authors thank Dr. Hao Lyu, Dr. Xiaokun Pei, Dr. Chang Yan, Dr. Sheena Louisia and Zichao Rong for helpful discussions. This work was supported by the U.S. Department of Energy, Office of Science, Office of Basic Energy Sciences, Materials Sciences and Engineering Division, under Contract No. DE-AC02-05-CH11231 within the Physical Chemistry of Inorganic Nanostructures Program (KC3103). Single-crystal X-ray Diffraction studies were performed at the UC Berkeley College of Chemistry X-ray Crystallography (CheXray). We thank Dr. Nick Settineri at UC Berkeley for their helps in SCXRD collection. Ultralow-frequency Raman spectroscopy was

performed at the Stanford Nano Shared Facilities (SNSF), supported by the National Science Foundation (ECCS-1542152). We thank Drs. Hasan Celik, Alicia Lund, and UC Berkeley's NMR facility in the College of Chemistry (CoC-NMR) for spectroscopic assistance. Instruments in the CoC-NMR are supported in part by NIH S10OD024998. J.J. and Y.Z. acknowledge the fellowship support from Suzhou Industrial Park. C.-K.L. acknowledges MOE Technologies Incubation Scholarship from Taiwan.

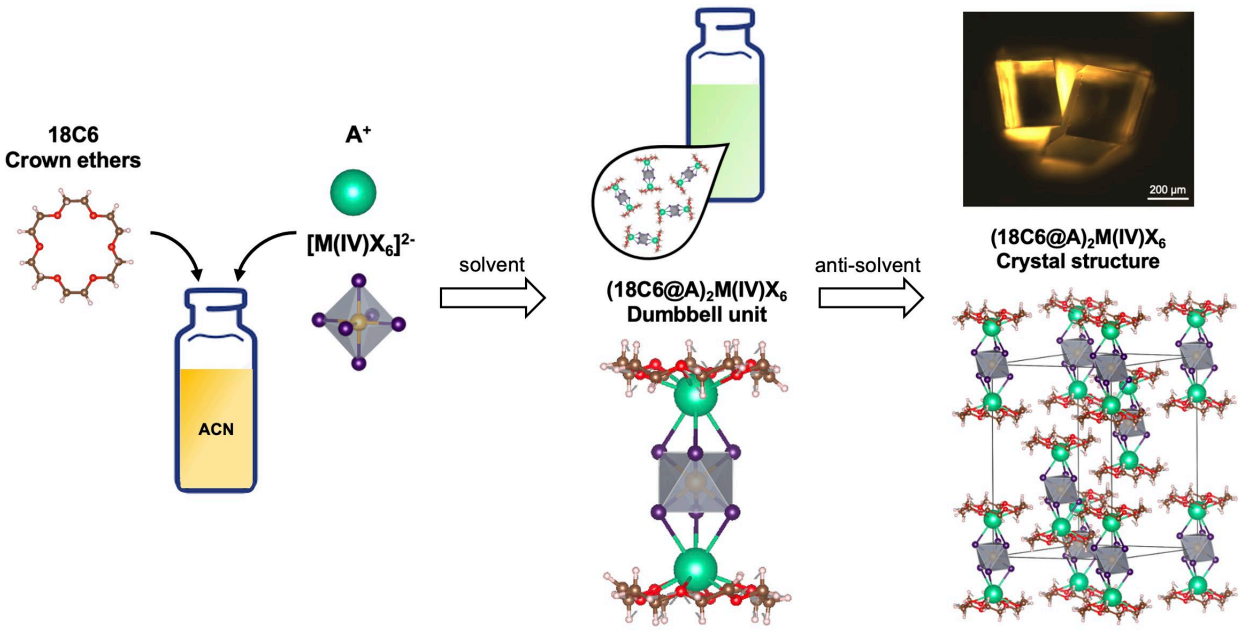

Figure 1. The supramolecular assembly strategy from $[M(IV)X_6]^{2-}$ octahedron to $(18C6@A)_2M(IV)X_6$. Dissolved alkali metal cation (A^+) and $[M(IV)X_6]^{2-}$ octahedron self-assemble into a dumbbell-shaped structural unit with crown ethers like 18-Crown-6 (18C6). The solution dispersed $(18C6@A)_2M(IV)X_6$ dumbbell structural units can further assemble into a rhombohedral packing single crystal. The dark field optical microscope image shows single crystals of $(18C6@Cs)_2Te(IV)Cl_6$.

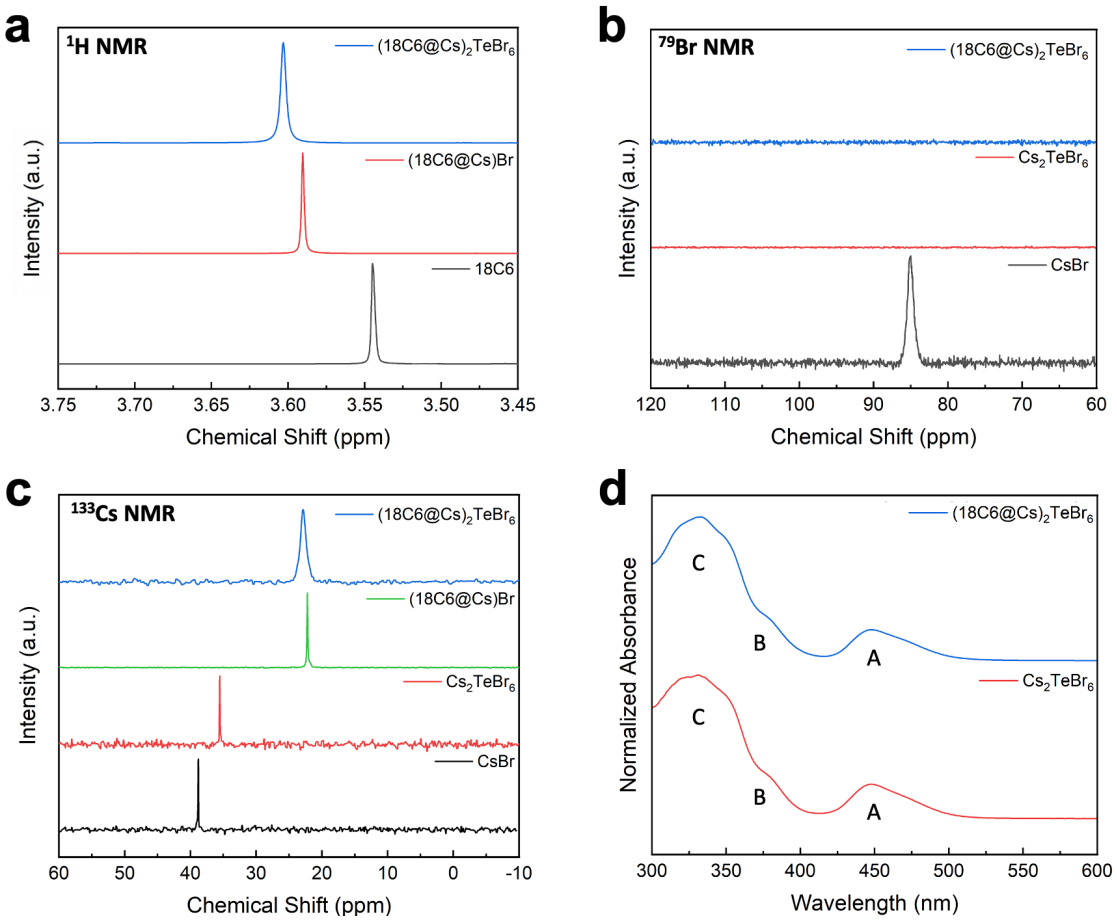

Figure 2. Evidence of the formation of (18C6@A)$_2$M(IV)X$_6$ dumbbell structural unit in solution. The composition of (18C6@Cs)$_2$TeBr$_6$ is applied as an illustrating example for the dumbbell structural unit, and acetonitrile (acetonitrile-d$_3$ for NMR) is used as the solvent. (a) ^{1}H NMR spectra for (18C6@Cs)$_2$TeBr$_6$ solution, and the control groups are (18C6@Cs)Br and 18C6 dissolved in solution. (b) ^{79}Br NMR spectra for (18C6@Cs)$_2$TeBr$_6$ solution, and the control groups are Cs$_2$TeBr$_6$ and CsBr dissolved in solution. (c) ^{133}Cs NMR spectra for (18C6@Cs)$_2$TeBr$_6$ solution, and the control groups are (18C6@Cs)Br, Cs$_2$TeBr$_6$ and CsBr dissolved in solution. (d) UV-vis spectra comparison of (18C6@Cs)$_2$TeBr$_6$ solution and Cs$_2$TeBr$_6$ dissolved in solution.

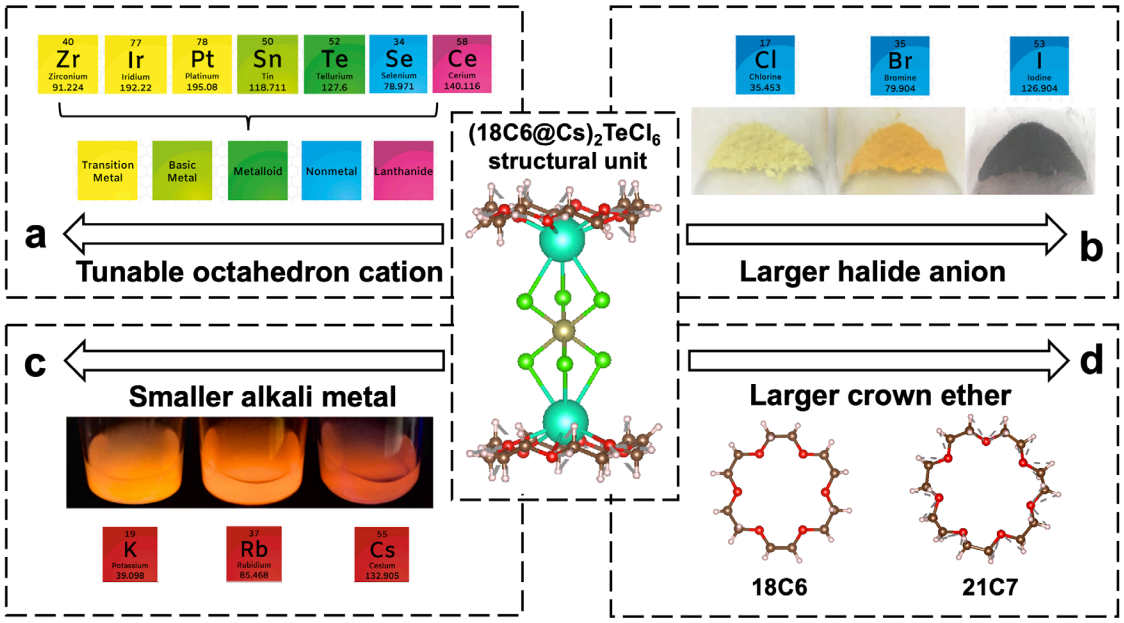

Figure 3. Synthetic tunability of the crown ether supramolecular approach. The four arrows represent the four dimensionalities in tuning the dumbbell structural unit from the initial $(18C6@Cs)_2TeCl_6$ structural unit: (a) seven tetravalent octahedra cations can be applied, including transition metal cations such as Zr^{4+}, Ir^{4+}, Pt^{4+}, basic metal cations such as Sn^{4+}, metalloid cations such as Te^{4+}, nonmetal cations such as Se^{4+}, and lanthanide cations such as Ce^{4+}; (b) tuning the halide anion from Cl^- to Br^- to I^-, and the optical images are the powders of $(18C6@Cs)_2TeX_6$ (X = Cl^-, Br^-, I^-) under ambient light; (c) modifying the alkali metal cation coupled with 18C6 from Cs^+ to Rb^+ to K^+, and the optical images are the powders of $(18C6@A)_2TeCl_6$ dispersed in an anti-solvent under UV lamp excitation; and (d) varying the size of the crown ether from 18C6 to 21C7.

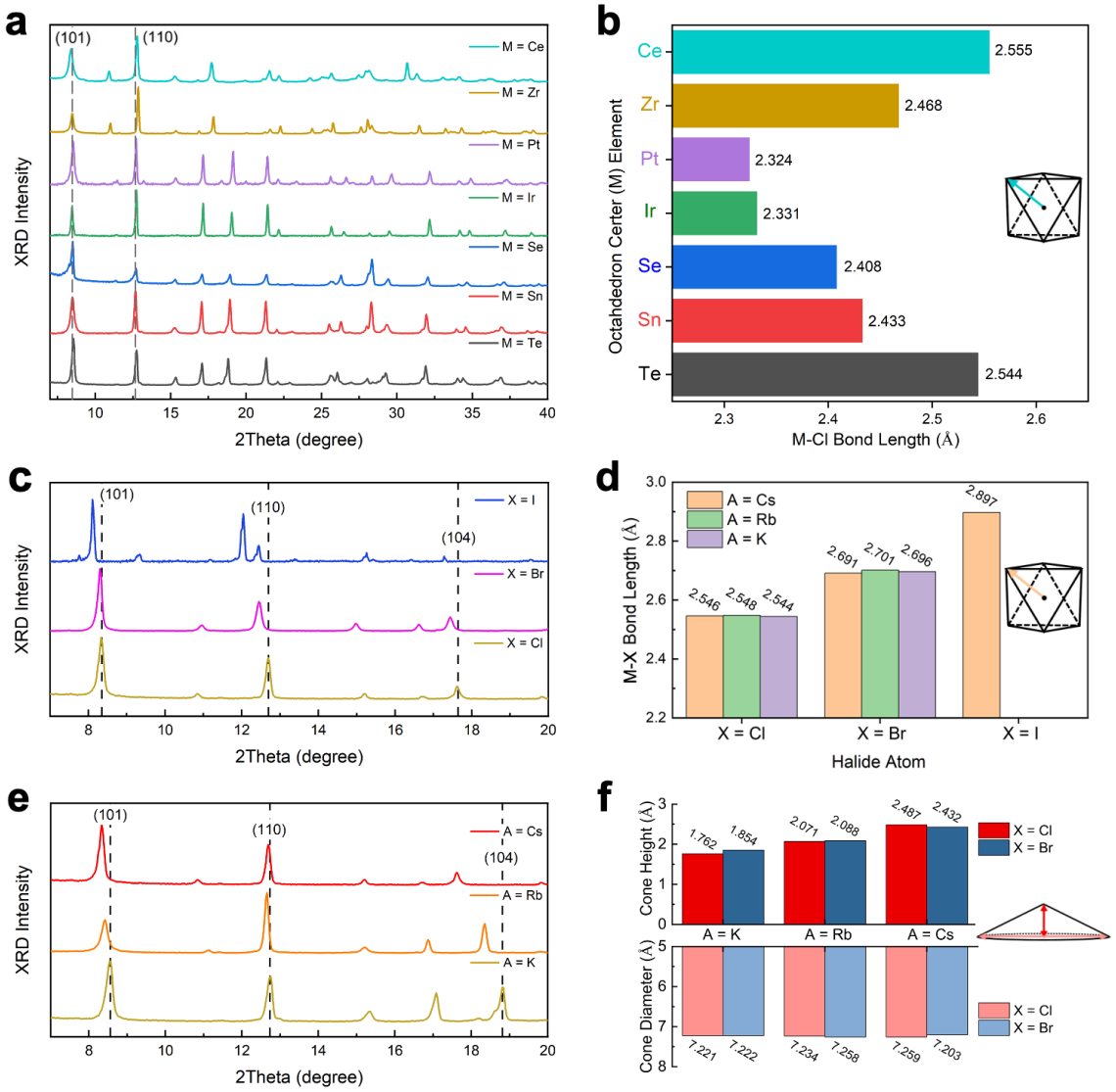

Figure 4. Systematic structural analysis of the family of $(18C6@A)_2M(IV)X_6$ crystals. Comparison of powder X-ray diffraction patterns by (a) tuning the octahedron center element (M) in $(18C6@A)_2M(IV)Cl_6$ (for M = Ce, Zr, A = Cs; for M = Pt, Ir, Se, Sn, Te, A = K); (c) changing the halide atom (X) in $(18C6@Cs)_2TeX_6$, and (e) varying the alkali metal atom (A) in $(18C6@A)_2TeCl_6$. Analysis of the geometric parameters of the dumbbell structural units: (b) the M-Cl bond length comparison of the structures with different octahedron center elements; (d) the M-X bond length increases with larger X; and (f) the height of the cone increases with larger A, while the diameter of the cone is insensitive to the change of A.

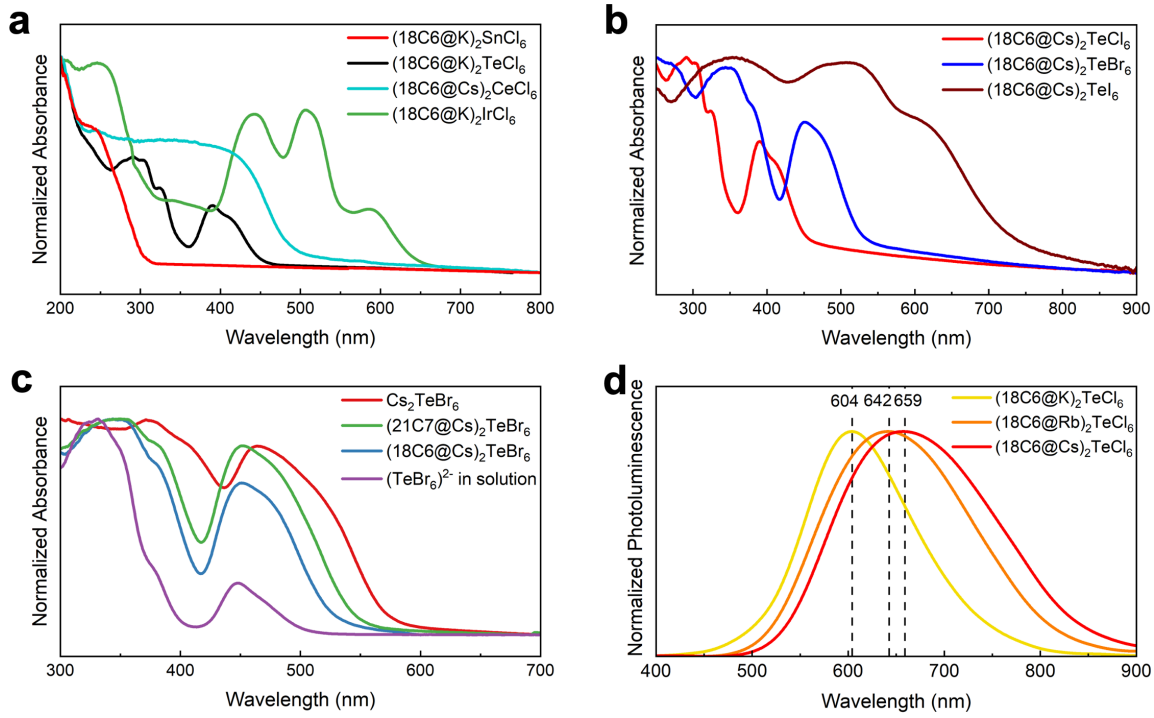

Figure 5. Optoelectronic tunability of the crown ether supramolecular approach. (a) Normalized UV-vis absorption spectra of $(18C6@A)_2M(IV)Cl_6$ ($M = Sn^{4+}$, Te^{4+}, Ce^{4+}, Ir^{4+}) crystals. (b) Normalized UV-vis absorption spectra of $(18C6@Cs)_2TeX_6$ ($X = Cl^-$, Br^-, I^-) crystals. (c) Normalized UV-vis absorption spectra of $[TeBr_6]^{2-}$ octahedra under four different packing geometries. (d) Normalized photoluminescence spectra of $(18C6@A)_2TeCl_6$ ($A = Cs^+$, Rb^+, K^+) crystals.

REFERENCES

(1) Protesescu, L.; Yakunin, S.; Bodnarchuk, M. I.; Krieg, F.; Caputo, R.; Hendon, C. H.; Yang, R. X.; Walsh, A.; Kovalenko, M. V. Nanocrystals of Cesium Lead Halide Perovskites (CsPbX(3), X = Cl, Br, and I): Novel Optoelectronic Materials Showing Bright Emission with Wide Color Gamut. *Nano Lett.* **2015**, *15*, 3692-3696.

(2) Kang, J., Wang, L. W. High Defect Tolerance in Lead Halide Perovskite $CsPbBr_3$. *J. Phys. Chem. Lett.* **2017**, *8*, 489-493.

(3) Kovalenko, M. V.; Protesescu, L.; Bodnarchuk, M. I. Properties and Potential Optoelectronic Applications of Lead Halide Perovskite Nanocrystals. *Science* **2017**, *358*, 745-750.

(4) Zhang, Y.; Saidaminov, M. I.; Dursun, I.; Yang, H.; Murali, B.; Alarousu, E.; Yengel, E.; Alshankiti, B. A.; Bakr, O. M.; Mohammed, O. F. Zero-Dimensional Cs_4PbBr_6 Perovskite Nanocrystals. *J. Phys. Chem. Lett.* **2017**, *8*, 961-965.

(5) Noel, N. K.; Abate, A.; Stranks, S. D.; Parrott, E. S.; Burlakov, V. M.; Goriely, A.; Snaith, H. J. Enhanced Photoluminescence and Solar Cell Performance via Lewis Base Passivation of Organic Inorganic Lead Halide Perovskites. *ACS Nano* **2014**, *8*, 9815-9821.

(6) Morad, V.; Yakunin, S.; Benin, B. M.; Shynkarenko, Y.; Grotevent, M. J.; Shorubalko, I.; Boehme, S. C.; Kovalenko, M. V. Hybrid 0D Antimony Halides as Air-Stable Luminophores for High Spatial-Resolution Remote Thermography. *Adv. Mater.* **2021**, *33*, 2007355.

(7) Boopathi, K. M.; Karuppuswamy, P.; Singh, A.; Hanmandlu, C.; Lin, L.; Abbas, S. A.; Chang, C. C.; Wang, P. C.; Li, G.; Chu, C. W. Solution-Processable Antimony-Based Light-Absorbing Materials Beyond Lead Halide Perovskites. *J. Mater. Chem. A* **2017**, *5*, 20843-20850.

(8) Sedakova, T. V.; Mirochnik, A. G.; Karasev, V. E. Structure and Luminescence Properties of Antimony (III) Complex Compounds. *Opt. Spectrosc.* **2008**, *105*, 517-523.

(9) Folgueras, M.; Jin, J.; Gao, M.; Quan, L.; Steele, J.; Srivastava, S.; Ross, M.; Zhang, R.; Seeler, F.; Schierle-Arndt, K.; Asta, M.; Yang, P. Lattice Dynamics and Optoelectronic Properties of Vacancy-Ordered Double Perovskite Cs_2TeX_6 ($X = Cl^-, Br^-, I^-$) Single Crystals. *J. Phys. Chem. C* **2021**, *125*, 25126-25139.

(10) Ju, D. X.; Zheng, X. P.; Yin, J.; Qiu, Z. W.; Turedi, B.; Liu, X. L.; Dang, Y. Y.; Cao, B. Q.; Mohammed, O. F.; Bakr, O. M.; Tao, X. T. Tellurium-Based Double Perovskites A_2TeX_6 with Tunable Band Gap and Long Carrier Diffusion Length for Optoelectronic Applications. *ACS Energy Letters* **2019**, *4*, 228-234.

(11) Nicholas, A. D.; Walusiak, B. W.; Garman, L. C.; Huda, M. N.; Cahill, C. L. Impact of Noncovalent Interactions on Structural and Photophysical Properties of Zero-Dimensional Tellurium (IV) Perovskites. *J. Mater. Chem. C* **2021**, *9*, 3271-3286.

(12) Zhou, J.; Luo, J.; Rong, X.; Wei, P.; Molokeev, M. S.; Huang, Y.; Zhao, J.; Liu, Q.; Zhang, X.; Tang, J.; Xia, Z. Lead-Free Perovskite Variant $Cs_2SnCl_{6-x}Br_x$ Single Crystals for Narrowband Photodetectors. *Adv. Opt. Mater.* **2019**, *7*, 1900139.

(13) Yin, H.; Chen, J.; Guan, P.; Zheng, D.; Kong, Q.; Yang, S.; Zhou, P.; Yang, B.; Pullerits, T.; Han, K. Controlling Photoluminescence and Photocatalysis Activities in Lead-Free $Cs_2Pt_xSn_{1-x}Cl_6$ Perovskites via Ion Substitution. *Angew Chem.* **2021**, *60*, 22693-22699.

(14) Jin, J.; Folgueras, M. C.; Gao, M.; Yu, S.; Louisia, S.; Zhang, Y.; Quan, L. N.; Chen, C.; Zhang, R.; Seeler, F.; Schierle-Arndt, K.; Yang, P. A New Perspective and Design Principle for Halide Perovskites: Ionic Octahedron Network (ION). *Nano Lett.* **2021**, *21*, 5415-5421.

(15) Gao, M.; Zhang, Y.; Lin, Z.; Jin, J.; Folgueras, M. C.; Yang, P. The Making of a Reconfigurable Semiconductor with a Soft Ionic Lattice. *Matter* **2021**, *4*, 3874-3896.

(16) Cram, D. J. The Design of Molecular Hosts, Guests, and Their Complexes. *Angew. Chem., Int. Ed. Engl.* **1988**, *27*, 1009-1112.

(17) Pedersen, C. J. The Discovery of Crown Ethers. *Angew. Chem.* **1988**, *100*, 1053-1059.

(18) Akutagawa, T.; Endo, D.; Noro, S. I.; Cronin, L.; Nakamura, T. Directing Organic-Inorganic hybrid Molecular-Assemblies of Polyoxometalate Crown-Ether Complexes with Supramolecular Cations. *Coord. Chem. Rev.* **2007**, *251*, 2547-2561.

(19) Morad, V.; Yakunin, S.; Kovalenko, M. V. Supramolecular Approach for Fine-Tuning of the Bright Luminescence from Zero-Dimensional Antimony (III) Halides. *ACS Mater. Lett.* **2020**, *2*, 845-852.

(20) Rogers, R. D.; Song, Y. The Crystal Structure of a Heterobimetallic Crown Ether Complex: [Na(dibenzo-18-crown-6)]-[$FeCl_4$]. *J. Chem. Crystallogr.* **1995**, *25*, 579-582.

(21) Hausmann, D.; Kuzmanoski, A.; Feldmann, C. $MnBr_2$/18-Crown-6 Coordination Complexes Showing High Room Temperature Luminescence and Quantum Yield. *Dalton Trans.* **2016**, *45*, 6541-6547.

(22) Folgueras, M. C.; Louisia, S.; Jin, J.; Gao, M.; Du, A.; Fakra, S. C.; Zhang, R; Seeler, F; Schrierle-Arndt, K.; Yang, P. Ligand-Free Processable Perovskite Semiconductor Ink. *Nano Lett.* **2021**, *21*, 8856-8862.

(23) Hopkins Jr, H. P.; Norman, A. B. Conductance and Infrared Studies on Acetonitrile Solutions Containing Crown Ethers and Alkali Metal Salts. *J. Phys. Chem.* **1980**, *84*, 309-314.

(24) Shamsipur, M.; Saeidi, M. Conductance Study of Binding of Some Rb^+ and Cs^+ Ions by Macrocyclic Polyethers in Acetonitrile Solution. *J. Solut. Chem.* **2000**, *29*, 1187-1198.

(25) Peng, L.; Clément, R. J.; Lin, M.; Yang, Y. CHAPTER 1:NMR Principles of Paramagnetic Materials, in NMR and MRI of Electrochemical Energy Storage Materials and Devices, **2021**, 1-70.

(26) Maughan, A. E.; Ganose, A. M.; Scanlon, D. O.; Neilson, J. R. Perspectives and Design Principles of Vacancy-Ordered Double Perovskite Halide Semiconductors. *Chem. Mater.* **2019**, *31*, 1184-1195.

(27) Faizan, M.; Bhamu, K.C.; Murtaza, G.; He, X.; Kulhari, N.; AL-Anazy, M.M.; Khan, S.H. Electronic and Optical Properties of Vacancy Ordered Double Perovskites A_2BX_6 (A= Rb, Cs; B= Sn, Pd, Pt; and X= Cl, Br, I): a First Principles Study. *Sci. Rep.* **2021**, *11*, 1-9.

(28) BelhajSalah, S.; Abdelbaky, M.S.; Garcia-Granda, S.; Essalah, K.; Nasr, C.B.; Mrad, M.L. Crystal Structure, Hirshfeld Surfaces Computational Study and Physicochemical Characterization of the Hybrid Material $(C_7H_{10}N)_2[SnCl_6]\cdot H_2O$. *J. Mol. Struct.* **2018**, *1152*, 276-286.

(29) Mathlouthi, M.; Valkonen, A.; Rzaigui, M.; Smirani, W. Structural Characterization, Spectroscopic, Thermal, AC Conductivity and Dielectric Properties and Antimicrobial Studies of $(C_8H_{12}N)_2[SnCl_6]$. *Phase Transitions* **2017**, *90*, 399-414.

(30) Tan, Z.; Chu, Y.; Chen, J.; Li, J.; Ji, G.; Niu, G.; Gao, L.; Xiao, Z.; Tang, J. Lead-Free Perovskite Variant Solid Solutions $Cs_2Sn_{1-x}Te_xCl_6$: Bright Luminescence and High Anti-Water Stability. *Adv. Mater.* **2020**, *32*, 2002443.

(31) Li, M.; Xia, Z. Recent Progress of Zero-Dimensional Luminescent Metal Halides. *Chem. Soc. Rev.* **2021**, *50*, 2626-2662.

(32) Hesse, K.; Gliemann, G. Magnetic Field Effect on the Luminescence of Octahedral Hexachloroselenate (IV). Evidence for the Vibronic Nature of the Low-Temperature Emission. *J. Phys. Chem.* **1991**, *95*, 95-98.

(33) Kaatz, T.; Marcovich, M. The Crystal Structure of the Compound Cs_2CeCl_6. *Acta Crystallogr.* **1966**, *21*, 1011-1011.

(34) Saeki, K.; Fujimoto, Y.; Koshimizu, M.; Yanagida, T.; Asai, K. Comparative Study of Scintillation Properties of Cs_2HfCl_6 and Cs_2ZrCl_6. *Appl. Phys. Express* **2016**, *9*, 042602.

(35) Khan, N.; Prishchenko, D.; Skourski, Y.; Mazurenko, V. G.; Tsirlin, A. A. Cubic Symmetry and Magnetic Frustration on the FCC Spin Lattice in K_2IrCl_6. *Phys. Rev. B* **2019**, *99*, 144425.

(36) Lin, Z.; Zhang, Y.; Gao, M.; Steele, J. A.; Louisia, S.; Yu, S.; Quan, L. N.; Lin, C.-K.; Limmer, D. T.; Yang, P. Kinetics of Moisture-Induced Phase Transformation in Inorganic Halide Perovskite. *Matter* **2021**, *4*, 2392-2402.

(37) Goldschmidt, V. M. Die Gesetze der Krystallochemie. *Naturwissenschaften* **1926**, *14*, 477-485.

(38) Vogler, A.; Nikol, H. The Structures of s^2 Metal Complexes in the Ground and sp Excited States. *Comments Inorg. Chem.* **1993**, *14*, 245-261.

(39) Yin, H.; Jin, Y.; Hertzog, J. E.; Mullane, K. C.; Carroll, P. J.; Manor, B. C.; Anna, J. M.; Schelter, E. J. The Hexachlorocerate (III) Anion: a Potent, Benchtop Stable, and Readily Available Ultraviolet Photosensitizer for Aryl Chlorides. *J. Am. Chem. Soc.* **2016**, *138*, 16266-16273.

(40) Machmer, P. On the Correlation of ^{35}Cl Nuclear Quadrupole Coupling Constants with $\pi \rightarrow \gamma 3$ and $\pi \rightarrow \gamma 5$ Optical Electron Transfer Bands of Transition Metal Complexes and its Significance in pi-Bonding. *Z. Naturforsch. B.* **1969**, *24*, 193-199.

(41) Boyer-Richard, S.; Katan, C.; Traore, B.; Scholz, R.; Jancu, J.-M.; Even, J. Symmetry-Based Tight Binding Modeling of Halide Perovskite Semiconductors. *J. Phys. Chem. Lett.* **2016**, *7*, 3833-3840.

(42) Biswas, A.; Bakthavatsalam, R.; Bahadur, V.; Biswas, C.; Mali, B. P.; Raavi, S. S. K.; Gonnade, R. G.; Kundu, J. Lead-Free Zero-Dimensional Tellurium (IV) Chloride-Organic Hybrid with Strong Room Temperature Emission as a Luminescent Material. *J. Mater. Chem. C* **2021**, *9*, 4351-4358.

(43) Steele, J. A.; Puech, P.; Keshavarz, M.; Yang, R.; Banerjee, S.; Debroye, E.; Kim, C. W.; Yuan, H.; Heo, N. H.; Vanacken, J.; Walsh, A.; Hofkens, J.; Roeffaers, M. B. J. Giant Electron-Phonon Coupling and Deep Conduction Band Resonance in Metal Halide Double Perovskite. *ACS Nano* **2018**, *12*, 8081-8090.

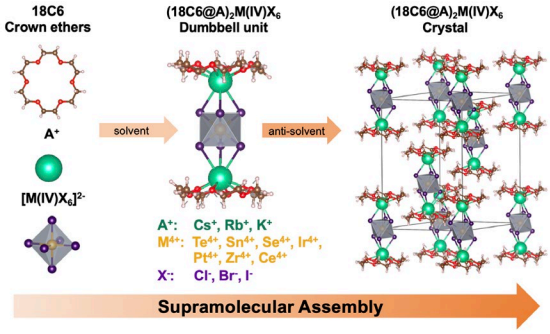

"TOC" graphics